

# Spatio-Temporal Detection of Cumulonimbus Clouds in Infrared Satellite Images

Ron Dorfman, Etai Wagner, Almog Lahav, Alon Amar, Ronen Talmon

The Viterbi Faculty of Electrical Engineering, Technion - Israel Institute of Technology

Haifa, Israel

Email: {rdorfman, etaiwag, salmogl}@campus.technion.ac.il

amar@technion.ac.il; ronon@ee.technion.ac.il

Yaron Halle

National Research Center

Haifa, Israel

**Abstract**—In this paper, we address the problem of Cumulonimbus (Cb) cloud detection from Infrared (IR) satellite images. The detection of such storm clouds is of high importance since they pose extreme danger to aviation. We present a joint spatio-temporal detection method that exploits the distinct spatial characteristics of Cb clouds as well as their prototypical evolution over time. The presented method is unsupervised and does not require labeled data or predefined spatial handcrafted features, such as particular shapes, temperatures, textures, and gradients. We demonstrate the performance of the proposed method on several sequences of IR satellite images taken from the middle east region.

## I. INTRODUCTION

Cb clouds are vertical and dense clouds associated with thunderstorms and atmospheric instability. They typically extend several kilometers vertically, from 200-4,000 meters up to 12,000 meters. In extreme cases, their peaks may even reach 21,000 meters. The extreme weather conditions characterizing Cb clouds make them a serious hazard for aviation. Therefore, monitoring Cb clouds is of high importance for avoiding flying into such danger zones.

Recently, several approaches for detection and localization of various clouds based on satellite images have been presented. Liu et al. proposed an artificial neural network (ANN) for cloud classification based on brightness temperature and intensity of three different IR channels [1], [2]. It was shown that this algorithm allows to track Cb evolution over time, yet it disregards the Cb temporal characteristics, i.e. the classification is carried out in each satellite image separately, leading to subpar performance. Conversely, Zhang et al. recently proposed to use temporal features, such as rotation and translation, for thunderstorm detection [3]. Based on these temporal features, combined with spatial features, a random forest classifier is trained using thunderstorm reports in the U.S. as a ground-truth.

These supervised methods are limited since they require a considerably large number of samples labeled either by experienced meteorologists, which is usually expensive and time-consuming procedure, or by some prior knowledge, which is often not available.

An unsupervised method presented by Berendes et al. classifies clouds using clustering based on spatial features such as intensity, channel differences and texture [4]. However,

this method has two significant disadvantages. First, it uses predefined handcrafted features that may not capture the true intrinsic properties of Cb clouds. Second, it ignores temporal information that can be extracted from a sequence of images.

In this paper, we propose an unsupervised method for Cb detection and localization based on joint space-time analysis of satellite images. By assuming that Cb clouds are rare phenomena in the entire image, we view them as spatial anomalies. Accordingly, we use a data-driven multiscale algorithm presented in [5], which allows for the detection of anomalies without explicitly describing in advance how these anomalies differ from the entire scene. Since Cb clouds are not only distinct in their spatial characteristics, but also in their evolution over time, we improve the Cb detection by incorporating features representing the typical radial expansion of the clouds. We demonstrate the advantage of our approach using several series of IR images taken from a geostationary satellite.

The remainder of the paper is organized as follows. In Section II, we formulate the problem. Section III and Section IV present the spatial and the temporal analysis, respectively. Section V describes the Cb cloud detection algorithm. In Section VI, we present the experimental results of our algorithm. Finally, Section VII concludes the paper.

## II. PROBLEM FORMULATION

Consider a time series of  $n$  IR images  $\{I_k\}_{k=1}^n$  acquired by a geostationary satellite, where  $k$  denotes the time index. An example for such image is presented in Fig. 1, where dark pixels represents low temperature.

Our goal is to detect and localize Cb clouds, such as the one pointed by a red arrow in Fig 1, in the given sequence of IR images. Specifically, for each image  $I_k$ , we aim to obtain a heat-map  $P_k$  of the same size as  $I_k$ , where larger values indicate more probable existence of a Cb cloud.

Let  $\Gamma_k$  be the set of all pixels in  $I_k$  containing a Cb cloud. Provided there exists a threshold  $\tau$  such that  $P_k(i, j) > \tau$  if and only if  $(i, j) \in \Gamma_k$ , Cb cloud detection and localization at the  $(i, j)$  pixel is given by:

$$T(i, j) = \begin{cases} 1, & P(i, j) > \tau \\ 0, & \text{otherwise} \end{cases} \quad (1)$$

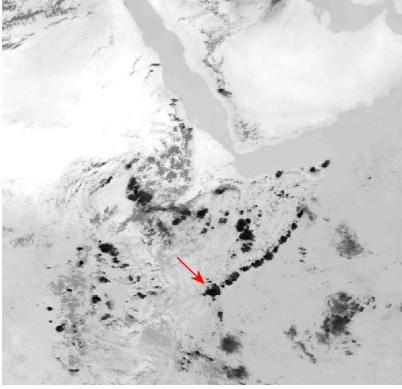


Fig. 1. Example of an image from the data set. A Cb cloud is indicated by a red arrow.

### III. SPATIAL ANOMALY DETECTION

The appearance of Cb clouds in satellite images is typically different from other types of clouds and as a result Cb clouds are visually noticeable. While some of the Cb discriminating features are explicitly defined and could be directly measured, e.g. its extreme low temperature, the vast majority of the features such as shape, texture and gradients are not definitive.

To overcome the lack of predefined discriminating features, we assume that Cb is a rare spatial phenomenon in the satellite image. Based on this assumption, we apply a data-driven anomaly detection method, facilitating the detection of Cb clouds without explicitly describing how these clouds differ from the entire scene. Following is a brief review of the main steps of the anomaly detection algorithm, proposed in [5].

Let  $p_i$  be a patch of size  $d \times d$  around the  $i$ -th pixel. Using diffusion maps [6], a dimension reduction method, we map each patch to a low-dimensional embedded space:

$$p_i \mapsto \varphi(p_i) \in \mathbb{R}^l, l < d^2 \quad (2)$$

The anomaly score of a patch  $p_i$  is defined by:

$$A(i) = 1 - \frac{1}{m} \sum_{j \in \mathcal{N}_i} \bar{w}(i, j) \quad (3)$$

where  $\mathcal{N}_i$  is the set of  $m$  nearest neighbors of  $p_i$  in the embedded space, and  $\bar{w}(i, j)$  is given by:

$$\bar{w}(i, j) = \exp\left(-\|\varphi(p_i) - \varphi(p_j)\|^2 / \bar{\sigma}\right) \quad (4)$$

To interpret the anomaly score definition in (3) we recall that the low-dimensional representation obtained by diffusion maps preserves local neighborhoods [6]. Therefore, if  $p_i$  is a normal patch with a large number of neighbors, then it is embedded into a dense neighborhood, and hence,  $A(i)$  is approximately zero. Conversely, if  $p_i$  is an abnormal patch, then it lies in a sparse neighborhood in the embedded space, and  $A(i)$  is approximately one.

The application of diffusion maps to images suffers from high computational complexity. Mishne and Cohen [5] presented an efficient multiscale method to compute diffusion maps that is based on a Gaussian pyramid representation [7].

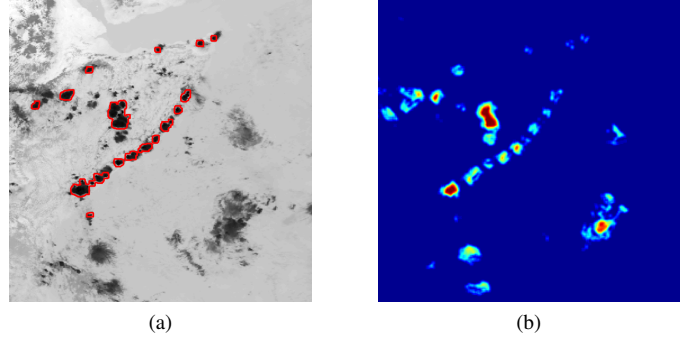


Fig. 2. Results of the spatial anomaly detection algorithm. (a) Zoom in of an input image with red contours indicating Cb clouds. (b) The anomaly score obtained by the algorithm.

The combination of a Gaussian pyramid and the existence of anomalies poses a challenge – since anomalies are by definition sparse, they could easily be excluded in the upsampling procedure, when transitioning from coarse to fine scales in the pyramid representation. In order to ensure that the anomalies are represented in each of the pyramid scales, the anomaly score  $A(i)$  (3) was incorporated into the upsampling procedure [5].

In addition to Cb clouds, an image may contain other spatial anomalies. Based on a priori knowledge about the low temperature of Cb clouds, we ignore irrelevant anomalies by replacing all pixels of high temperature with Gaussian noise.

Figure 2 presents the results of the anomaly detection algorithm described above. Figure 2(a) shows a part of the input image, where the Cb clouds are indicated by red contours. Figure 2(b) presents the anomaly score as an image, where pixels attaining high anomaly score appear in red and pixels attaining low anomaly score appear in blue. We observe that the algorithm indeed detected few of the Cb clouds in the image, but many of the Cb clouds, especially the small ones, are missed.

### IV. TEMPORAL ANOMALY DETECTION

In addition to their spatial diversity, Cb clouds differ from other types of clouds in terms of their temporal evolution. During the formation of a Cb cloud, it propagates upward, typically stretching to high altitudes. When the propagation reaches the Tropopause, which is a stable high-altitude atmospheric layer, they cannot continue to develop upward, and then, the top of the clouds spread out and form an anvil shape. In a sequence of satellite images, it is seen as an outward expansion. An example of this phenomenon is demonstrated in Fig. 3, where three consecutive images of the same Cb cloud propagation are presented with a 15 minute time difference between them.

Following is a description of our method for the quantification of the radial expansion characterizing Cb clouds. Consider a 2D vector field  $\mathbf{F}(x, y)$  representing the motion of objects in two consecutive images:

$$\mathbf{F}(x, y) = F_x(x, y) \cdot \hat{x} + F_y(x, y) \cdot \hat{y}$$

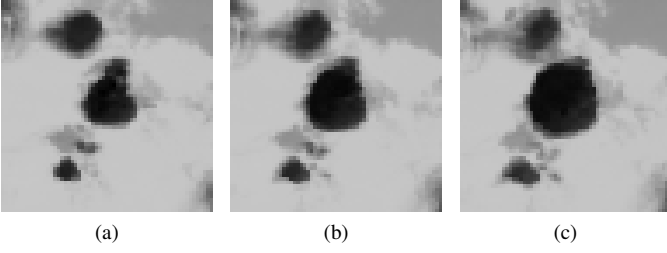


Fig. 3. The evolution of a Cb cloud over time in three different time steps, where the time difference between two consecutive images is 15 minutes. The earliest image is depicted in (a) and the latest in (c).

where  $x$  and  $y$  denote the axes and  $\hat{x}$  and  $\hat{y}$  their respective unit vector directions. Given a compact part of the image denoted by  $A$ , the flux passing through its boundary  $C$  is defined by:

$$\text{flux}(\mathbf{F}, A) := \oint_C (\mathbf{F} \cdot \hat{\mathbf{n}}) dc \quad (5)$$

where  $\hat{\mathbf{n}}$  is the normal to the boundary. If  $A$  represents a cloud, and it is expanded radially in two consecutive images, then the vector field  $\mathbf{F}$  approximately coincides with the normal of  $C$ . Therefore we expect a significant flux for a cloud with outward expansion. Conversely, other motions, e.g. translation, where  $\mathbf{F}$  is constant along  $C$ , results in a negligible flux.

We compute the flux in (5) by using the divergence theorem:

$$\iint_A (\nabla \cdot \mathbf{F}) da = \oint_C (\mathbf{F} \cdot \hat{\mathbf{n}}) dc \quad (6)$$

To derive a discrete form of (6), we define the discrete vector field:

$$\hat{\mathbf{F}}(i, j) = F_n(i, j) \cdot \hat{\mathbf{n}} + F_m(i, j) \cdot \hat{\mathbf{m}}$$

and the discrete divergence of  $\hat{\mathbf{F}}$  at the  $(i, j)$  pixel:

$$\text{div}\{\hat{\mathbf{F}}\}(i, j) = \frac{1}{2} \left[ \left( F_n(i+1, j) - F_n(i-1, j) \right) + \left( F_m(i, j+1) - F_m(i, j-1) \right) \right]$$

Accordingly, the discrete flux passing through a segment  $S$  in the image is given by:

$$\text{flux}(\hat{\mathbf{F}}, S) = \sum_{(i,j) \in S} \text{div}\{\hat{\mathbf{F}}\}(i, j) \quad (7)$$

For the computation of  $\hat{\mathbf{F}}$  given two images  $(I_{m-d}, I_m)$ , we use the exhaustive block matching method implemented in Computer Vision System Toolbox of Matlab. For each patch in  $I_{m-d}$ , this method computes  $\hat{\mathbf{F}}$  by finding the most similar patch in  $I_m$  among a predefined set of possible neighbors. To divide the image into segments we apply the watershed segmentation method [8] to the gradient magnitude image of  $I_m$ , after a preprocessing described in Matlab documentation for this method. We denote the flux image computed according to (7) by  $\Phi$ .

Figure 4 illustrates the computation of the flux image  $\Phi$  for two different clouds: Cb (top) and Cirrus (Ci) (bottom). Similarly to Cb clouds, Ci clouds are characterized by low

temperatures. As a result, the distinction between them based only on spatial information from the IR image is a challenging task. Figure 4(a) and Fig. 4(d) show the input image  $I_m$  of a Cb cloud and a Ci cloud, respectively. Figure 4(b) and Fig. 4(e) present the vector field  $\hat{\mathbf{F}}$  computed from two consecutive images with a time difference of an hour. For illustration purposes, we depict the input images  $I_m$  and  $I_{m-d}$  in the background of the vector field  $\hat{\mathbf{F}}$  in yellow and blue colors, respectively. It can be visually observed that arrows in the Cb cloud boundary point outward, in contrast to the arrows in the Ci cloud boundary. Figure 4(c) and Fig. 4(f) present the flux image  $\Phi$ , computed by (7) using the vector field  $\hat{\mathbf{F}}$ . We observe that the flux computed in the segment containing a Cb cloud is significantly higher compared with other segments in Fig. 4(c), or with the segment containing the Ci cloud in Fig. 4(f). This example demonstrates how we translate the characteristic temporal evolution of Cb clouds to a measurable feature, which can contribute to the distinction of Cb clouds.

## V. CB CLOUD DETECTION

The spatial anomaly detection algorithm, described in Section III is based on the anomaly score (3) of a patch  $p_i$ . Here, we propose a new score particularly designed for the detection of Cb clouds, which incorporates both the spatial and the temporal features of the Cb clouds. The new score, termed the Cb score, of a patch  $p_i$  at the  $\ell$ -th scale of the Gaussian pyramid [5] is defined by

$$C^{[\ell]}(i) = \alpha \cdot \Phi^{[\ell]}(i) + (1 - \alpha) \cdot A^{[\ell]}(i) \quad (8)$$

where  $\Phi^{[\ell]}$  is the flux image, produced as described in Section IV, down-sampled and normalized to  $[0, 1]$ , and  $A^{[\ell]}$  is the anomaly score, both at the  $\ell$ -th scale.  $\alpha \in [0, 1]$  is a hyperparameter determines the relative weight of the temporal feature and the spatial feature.

Given two frames  $(I_{m-d}, I_m)$ , we compute the normalized flux image  $\Phi$  and apply the multiscale anomaly detection algorithm described in Section III to the image  $I_m$  with an important modification – the anomaly score  $A^{[\ell]}$  is replaced with the new Cb score  $C^{[\ell]}$ . The Cb score at the finest scale,  $C^{[0]}$ , determines the detection of Cb clouds in  $I_m$ . We apply a threshold  $\tau$  to  $C^{[0]}$  in order to get a binary image  $T$ , indicating which pixels belong to Cb clouds. This detection procedure is summarised in Algorithm 1.

Since the normalized flux image  $\Phi$  highly depends on the selected time step  $d$ , we repeat Algorithm 1 over  $K$  consecutive time steps. Consider a set with  $K$  pairs of frames  $\{(I_{m-d+k}, I_{m+k})\}_{k=0}^{K-1}$ . For every pair, we apply Algorithm 1, obtaining  $K$  output images  $\{C_k^{[0]}\}_{k=0}^{K-1}$ . We then apply a threshold  $\tau$  to every image to get a set of binary images  $\{T_k\}_{k=0}^{K-1}$ , such that:

$$T_k(i) = \begin{cases} 1, & C_k^{[0]}(i) > \tau \\ 0, & \text{otherwise} \end{cases} \quad (9)$$

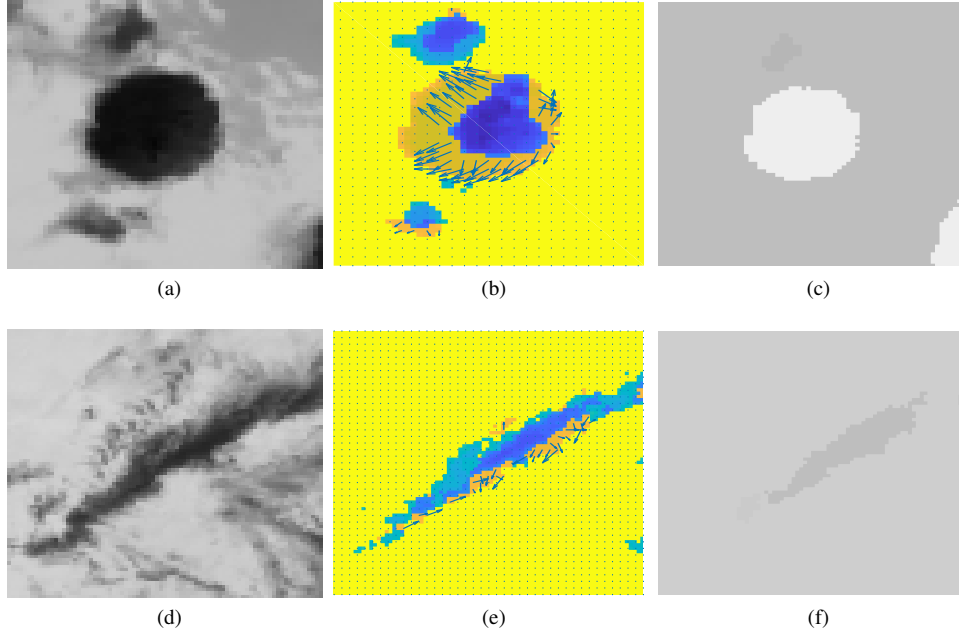


Fig. 4. Illustration of flux computation. The arrows in (b), (e) represents the vector fields of the Cb cloud and the Ci cloud in (a), (d), respectively, which are constructed with respect to previous images from an hour before. (c), (f) are the corresponding flux images. The flux through the Cb cloud is significantly larger compared to the Ci cloud.

Finally, we generate a single binary output image  $\tilde{T}$  via the following pixel wise 'OR' operation:

$$\tilde{T}(i) = \begin{cases} 1, & \text{if } \exists k \in \{0, \dots, K-1\} \text{ s.t. } T_k(i) = 1 \\ 0, & \text{otherwise} \end{cases} \quad (10)$$

## VI. EXPERIMENTAL RESULTS

To evaluate our method, we use 6 sequences of IR images. Each sequence comprises 8 images recorded with a time difference of 15 minutes. The size of each image is  $1024 \times 1024$ , where each pixel represents a temperature ranging from  $-80$  to  $47.5^\circ\text{C}$ . All images were labeled by an expert meteorologist: these labels were considered our ground truth.

The parameters of our algorithm are configured as follows. A typical duration of Cb cloud is approximately two hours. Therefore, to capture its characteristic evaluation, we set the time difference between two images required for the flux computation to be half of the typical duration, i.e. one hour. The number of image pairs is  $K = 4$ , such that the entire duration of Cb is covered. For the Gaussian pyramid presented in Section 3, we use  $L = 3$  scales. On one hand, using coarser scales would reduce the computational complexity. On the other hand, further down-sampling would eliminate small Cb clouds. The temporal feature weight in (8) is set to be 0.2. We chose this value experimentally.

We compare Algorithm 1 to three different methods. First, we apply thresholding such that all the pixels under some temperature are considered a Cb cloud. The second method is the spatial anomaly detection described in Section III. The third method is the spatio-temporal Cb detection described

---

### Algorithm 1: Spatio-temporal Cb detection

---

**Input:** Two images  $(I_{m-d}, I_m)$ , the number of pyramid scales  $L$ , and a weighting parameter  $\alpha$ .

- 1 Construct a Gaussian pyramid of  $L$  scales of  $I_m$ ,  $\{I_m^{[\ell]}\}_{\ell=0}^{L-1}$
- 2 Compute the flux image  $\Phi$  between the input images  $(I_{m-d}, I_m)$
- 3 Construct a Gaussian pyramid of  $L$  scales of  $\Phi$ ,  $\{\Phi^{[\ell]}\}_{\ell=0}^{L-1}$
- 4 Initialize a set  $\Gamma$  with random subset of patches from  $I_m^{[L-1]}$
- 5 **for**  $\ell \leftarrow L-1$  **to** 0 **do**
- 6     Compute the anomaly score  $A^{[\ell]}$  of the patches of  $I_m^{[\ell]}$  by applying anomaly detection to  $\Gamma$  as in [5].
- 7     Compute the Cb score:  
 $C^{[\ell]} = \alpha \cdot \Phi^{[\ell]} + (1 - \alpha) \cdot A^{[\ell]}$
- 8     **if**  $\ell \neq 0$  **then**
- 9         Empty  $\Gamma$
- 10         Apply a threshold to the Cb score and obtain suspicious patches of  $I_m^{[\ell-1]}$
- 11         Add the suspicious patches to  $\Gamma$
- 12         Add random patches of  $I_m^{[\ell-1]}$  to  $\Gamma$
- 13     **end**
- 14 **end**

---

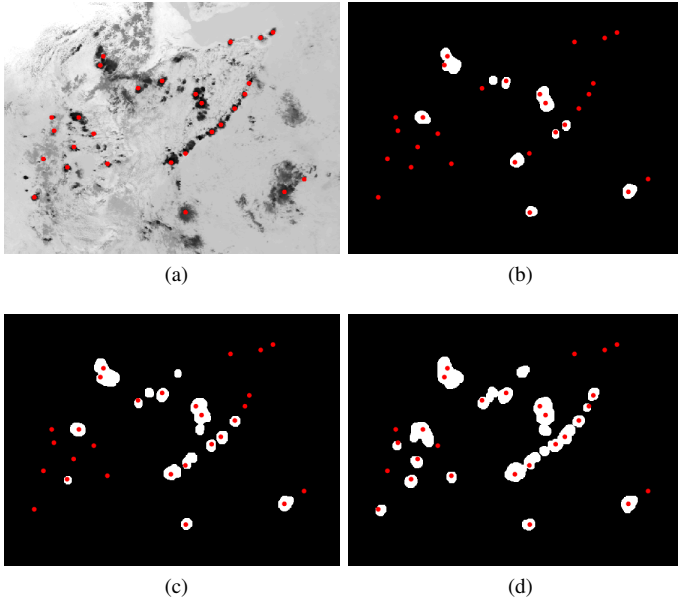


Fig. 5. Visual comparison between the output obtained by different algorithms. (a) A cropped version of the input image. (b) The output when applying a threshold to the spatial detection algorithm. (c) The result of Algorithm 1 with  $K = 1$ . (d) The result of Algorithm 1 with  $K = 4$ .

in Section IV with a single time step, i.e. Algorithm 1 with  $K = 1$ .

Figure 5(a) presents one input image together with red points representing the Cb clouds labeled by an expert meteorologist. Figures 5(b)-(d) compare the detection results of the three different methods: spatial anomaly detection (Fig. 5(b)), Algorithm 1 with  $K = 1$  (Fig. 5(c)), and Algorithm 1 with  $K = 4$  (Fig. 5(d)). White regions in these figures represent Cb clouds. Figure 5 shows that the spatio-temporal anomaly detection with multi time steps described in Algorithm 1 obtains higher detection rate than the other methods.

We note that a primary challenge in all of the above methods is the configuration of the decision threshold  $\tau$  in (9). A low threshold results in high detection rate, but may lead to many false-alarms. Decreasing the threshold would reduce the false-alarms, yet it would increase the number of undetected Cb clouds.

To find a pleasing value for  $\tau$ , we sampled different values and constructed a precision recall curve shown in Fig. 6. Each point on the curve represents a different threshold value and is calculated through averaging over all examples. It can be clearly seen that over 50% recall our solution vastly outperforms all other approaches at every point keeping a high precision rate. High precision values in the very low recall region appear because for low thresholds all clouds are considered Cb. This results in a high true positive result but also a high false positive count.

## VII. CONCLUSIONS

In this paper we addressed the problem of Cb clouds detection in IR satellite images. We presented a joint space-

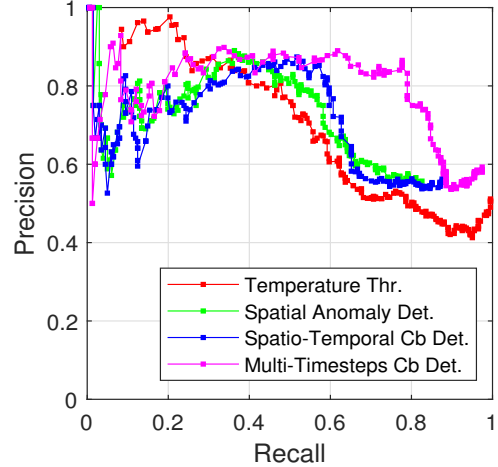


Fig. 6. Precision of the detection vs recall. Each point specifies a different threshold value.

time analysis framework, combining temporal features into a multiscale spatial anomaly detection algorithm. Our approach is completely unsupervised and does not require explicit predefined spatial features. We showed that the addition of the temporal features is important, and that improved results are obtained compared to the spatial anomaly detection algorithm alone. Moreover, the proposed detection is based on multiple time steps, which significantly improved the detection rates compared to merely a single time step.

## ACKNOWLEDGMENT

The authors would like to thank Nimrod Peleg, Yair Moshe and the Signal and Image Processing Lab (SIPL) staff for their support and helpful suggestions.

## REFERENCES

- [1] Y. Liu, D.-G. Xi, Z.-L. Li, and C.-X. Shi, "Automatic tracking and characterization of cumulonimbus clouds from fy-2c geostationary meteorological satellite images," *Advances in Meteorology*, vol. 2014, 2014.
- [2] Y. Liu, J. Xia, C.-X. Shi, and Y. Hong, "An improved cloud classification algorithm for china's fy-2c multi-channel images using artificial neural network," *Sensors*, vol. 9, no. 7, pp. 5558–5579, 2009.
- [3] Y. Zhang, S. Wistar, J. Li, M. A. Steinberg, and J. Z. Wang, "Severe thunderstorm detection by visual learning using satellite images," *IEEE Transactions on Geoscience and Remote Sensing*, vol. 55, no. 2, pp. 1039–1052, 2017.
- [4] T. A. Berendes, J. R. Mecikalski, W. M. MacKenzie, K. M. Bedka, and U. Nair, "Convective cloud identification and classification in daytime satellite imagery using standard deviation limited adaptive clustering," *Journal of Geophysical Research: Atmospheres*, vol. 113, no. D20, 2008.
- [5] G. Mishne and I. Cohen, "Multiscale anomaly detection using diffusion maps," *IEEE Journal of selected topics in signal processing*, vol. 7, no. 1, pp. 111–123, 2013.
- [6] R. R. Coifman and S. Lafon, "Diffusion maps," *Applied and computational harmonic analysis*, vol. 21, no. 1, pp. 5–30, 2006.
- [7] P. J. Burt and E. H. Adelson, "The laplacian pyramid as a compact image code," in *Readings in Computer Vision*. Elsevier, 1987, pp. 671–679.
- [8] S. Beucher and F. Meyer, "The morphological approach to segmentation: the watershed transformation," *Optical Engineering-New York-Marcel Dekker Incorporated-*, vol. 34, pp. 433–433, 1992.